

Discontinuous Galerkin Time Domain (DGTD) Methods for the Study of 2-D Waveguide-Coupled Microring Resonators

Xia Ji, Tiao Lu, Wei Cai, *Senior Member, IEEE*, and Pingwen Zhang

Abstract—This paper presents the study of coupling efficiencies between two-dimensional (2-D) waveguides and microring resonators with a newly developed high-order discontinuous Galerkin time domain (DGTD) method for Maxwell's equations. The DGTD method is based on a unified formulation for the physical media and the artificial media in the uniaxial perfectly matched layer (UPML) regions used to truncate the computational domain. The DGTD method employs finite element type meshes and uses piecewise high-order polynomials for spatial discretization of the Maxwell's equations and Runge–Kutta methods for time integration. After demonstrating the high-order convergence of the DGTD method, the effect of separation gap between the waveguides and one and two microrings on the coupling efficiency and transmittance for pulse propagations is studied.

Index Terms—Discontinuous Galerkin time domain (DGTD), Maxwell's equations, microring resonators, uniaxial perfectly matched layer (UPML).

I. INTRODUCTION

OPTICAL microring resonators, well known for their extremely high-quality factors [1]–[3], provide potential applications in all-optical network devices such as ultranarrowband and large free spectral range channel dropping filters [4]. Many analytical methods have been used to model microring resonators, such as the scattering matrix approach [5], the method of conformal mapping [6], the coupled mode theory [7], etc. Numerical method provides an indispensable approach once the devices to be modeled are too complicated as the analytic methods become inapplicable or intractable. The finite difference time domain (FDTD) approach based on the traditional Yee's scheme for microring resonators have been discussed in [8] and was used for the computation of whispering gallery modes (WGMs) [9]. In [10], a finite element method is used to analyze the WGM in anisotropic dielectric resonators.

In this paper, a discontinuous Galerkin time domain (DGTD) method [14] will be applied to simulate the coupling between

waveguides and microring resonators. To the authors' knowledge, this is the first time to apply DGTD to study such a device. The DGTD used in this paper was developed recently for dispersive media and the uniaxial perfectly matched layer (UPML) regions that are used to truncate the computational domain [11]. Careful comparison between the DGTD and FDTD is also given in [11] for the scattering of dielectric objects. The main advantages of the DGTD method are the high-order accuracy even in the presence of material interface (the accuracy of the FDTD method with Yee's scheme will degenerate into first order), phase-preserving properties, and easy parallel implementation. Even for discontinuous field, exponential convergence with respect to the order of the basis functions can be obtained with the DGTD methods [11]. Such high-order convergence will be demonstrated in this paper for the calculation of coupling efficiency and transmittance for the coupling of waveguides and microrings. In [12], the successful optical transfer between microcylinders with the DGTD method has already been demonstrated. In this paper, the authors will simulate how the resonant modes can be excited by the incoupling via a waveguide and also the out-coupling to an output waveguide.

The remaining part of the paper is organized as follows. In Section II, a unified formulation for the Maxwell's equations for microring resonators in physical regions and UPML regions is given. The DGTD method with the definition of numerical flux is proposed in Section III. In Section IV, the numerical convergence of the proposed DGTD method is first studied and then applied to the coupling and transmission properties of two-dimensional (2-D) one- and two-microring resonators. Finally, a conclusion is given in Section V.

II. UNIFIED FORMULATION OF MAXWELL'S EQUATIONS IN PHYSICAL AND UPML REGIONS

We consider a nondimensionalized form of Maxwell equations for both transverse electric (TE) and transverse magnetic (TM) cases in physical regions and UPML regions [11] by introducing nondimensionalized variables

$$\frac{x}{L} \rightarrow x, \quad \frac{y}{L} \rightarrow y, \quad \frac{ct}{L} \rightarrow t, \quad Z_0 \mathbf{H} \rightarrow \mathbf{H}, \quad \mathbf{E} \rightarrow \mathbf{E} \quad (1)$$

where L is the reference length associated with a given problem; in this paper, we set $L = 1 \mu\text{m}$, c is the speed of light in free space, and $Z_0 = \sqrt{\mu_0/\epsilon_0}$ is the free-space impedance. In

Manuscript received October 14, 2004; revised May 3, 2005. The work of W. Cai was supported partially by the U.S. National Science Foundation (Grant DMS-0408309) and the U.S. Department of Energy (Grant DE-FG05-94ER253519), while the work of P. Zhang was supported by the National Science Foundation of China 90207009 and the Distinguished Young Scholars 10225103.

X. Ji, T. Lu, and P. Zhang are with the LMAM and School of Mathematical Sciences, Peking University, Beijing 100871, China (e-mail: pzhang@pku.edu.cn).

W. Cai is with the Department of Mathematics, Center for Optoelectronics and Optical Communications, University of North Carolina at Charlotte, Charlotte, NC 28223 USA (e-mail: wcai@uncc.edu).

Digital Object Identifier 10.1109/JLT.2005.855858

the UPML region, we introduce the polarization variables P^m , Q_x^m , and Q_y^m for the TM case and P^e , Q_x^e , and Q_y^e for the TE case. Here, the TE case refers to a situation where the magnetic field has only one component, while two electric fields exist on the plane transverse to the magnetic field. The TM case is defined similarly.

1) TM case

$$\begin{aligned} \epsilon_r \frac{\partial E_z}{\partial t} &= \frac{\partial H_y}{\partial x} - \frac{\partial H_x}{\partial y} - \epsilon_r(\sigma_x + \sigma_y)E_z + P^m \\ \mu_r \frac{\partial H_x}{\partial t} &= -\frac{\partial E_z}{\partial y} - \mu_r(\sigma_y - \sigma_x)H_x + Q_x^m \\ \mu_r \frac{\partial H_y}{\partial t} &= \frac{\partial E_z}{\partial x} - \mu_r(\sigma_x - \sigma_y)H_y + Q_y^m \\ \frac{\partial P^m}{\partial t} &= -\epsilon_r \sigma_x \sigma_y E_z \\ \frac{\partial Q_x^m}{\partial t} &= -\sigma_x Q_x^m + \mu_r \sigma_x (\sigma_y - \sigma_x) H_x \\ \frac{\partial Q_y^m}{\partial t} &= -\sigma_y Q_y^m + \mu_r \sigma_y (\sigma_x - \sigma_y) H_y. \end{aligned} \quad (2)$$

2) TE case

$$\begin{aligned} \mu_r \frac{\partial H_z}{\partial t} &= -\frac{\partial E_y}{\partial x} + \frac{\partial E_x}{\partial y} - \mu_r(\sigma_x + \sigma_y)H_z - P^e \\ \epsilon_r \frac{\partial E_x}{\partial t} &= \frac{\partial H_z}{\partial y} - \epsilon_r(\sigma_y - \sigma_x)E_x - Q_x^e \\ \epsilon_r \frac{\partial E_y}{\partial t} &= -\frac{\partial H_z}{\partial x} - \epsilon_r(\sigma_x - \sigma_y)E_y - Q_y^e \\ \frac{\partial P^e}{\partial t} &= \mu_r \sigma_x \sigma_y H_z \\ \frac{\partial Q_x^e}{\partial t} &= -\sigma_x Q_x^e - \epsilon_r \sigma_x (\sigma_y - \sigma_x) E_x \\ \frac{\partial Q_y^e}{\partial t} &= -\sigma_y Q_y^e - \epsilon_r \sigma_y (\sigma_x - \sigma_y) E_y. \end{aligned} \quad (3)$$

The derivation of these equations can be found in [11]. When the UPML parameters $\sigma_x = 0$ and $\sigma_y = 0$, the above equations are reduced to the normal Maxwell's equations in the physical media. The P 's and Q 's above are the auxiliary polarization variables used to handle the temporal convolution of the electromagnetic fields of the UPML regions. The UPML losses $\sigma_x(x)$ is usually set to have a polynomial profile [15]

$$\sigma_x(x) = \left(\frac{l}{d}\right)^m \sigma_{x,max} \quad (4)$$

where l is the distance away from the interface between the UPML and the physical solution domain, and d is the thickness of the UPML. The definition of $\sigma_y(y)$ is similar. The reflection factor for the UPML can be found to be [15]

$$R(\theta) = e^{-\frac{2\eta\sigma_{x,max}d\cos\theta}{\epsilon_r(m+1)}} \quad (5)$$

where θ is the incident angle, and η is the UPML's characteristic wave impedance.

Considering the TM case, we set $\mathbf{U} = (\epsilon_r E_z, \mu_r H_x, \mu_r H_y, P^m, Q_x^m, Q_y^m)^T$, the conservation form for \mathbf{U} is

$$\frac{\partial \mathbf{U}}{\partial t} + \nabla \cdot (\bar{\mathbb{A}}\mathbf{U}) = \mathbf{S} \quad (6)$$

where $\bar{\mathbb{A}}$ and \mathbf{S} are given below. The fourth to sixth equations in (2) are actually ordinary differential equations, and thus, we can rewrite the conservation system as

$$\frac{\partial \mathbf{U}^{(1)}}{\partial t} + \nabla \cdot (\mathbb{A}\mathbf{U}^{(1)}) = \mathbf{S}^{(1)} \quad (7)$$

$$\frac{\partial \mathbf{U}^{(2)}}{\partial t} = \mathbf{S}^{(2)} \quad (8)$$

where $\mathbf{U}^{(1)} = (\epsilon_r E_z, \mu_r H_x, \mu_r H_y)^T$, $\mathbf{U}^{(2)} = (P^m, Q_x^m, Q_y^m)^T$, $\mathbf{U} = (\mathbf{U}^{(1)}, \mathbf{U}^{(2)})^T$, $\mathbf{S} = (\mathbf{S}^{(1)}, \mathbf{S}^{(2)})^T$, and $\mathbb{A} = (A_x, A_y)$, where

$$A_x = \begin{pmatrix} 0 & 0 & -\frac{1}{\mu_r} \\ 0 & 0 & 0 \\ -\frac{1}{\epsilon_r} & 0 & 0 \end{pmatrix} \quad (9)$$

$$A_y = \begin{pmatrix} 0 & \frac{1}{\mu_r} & 0 \\ \frac{1}{\epsilon_r} & 0 & 0 \\ 0 & 0 & 0 \end{pmatrix}. \quad (10)$$

$\bar{\mathbb{A}}$ is given as

$$\bar{\mathbb{A}} = (\bar{A}_x, \bar{A}_y)$$

where

$$\bar{A}_x = \begin{pmatrix} A_x & 0_{3 \times 3} \\ 0_{3 \times 3} & 0_{3 \times 3} \end{pmatrix}, \quad \bar{A}_y = \begin{pmatrix} A_y & 0_{3 \times 3} \\ 0_{3 \times 3} & 0_{3 \times 3} \end{pmatrix}.$$

Here, $0_{n \times m}$ denotes zero matrix with n rows and m columns. The source terms $\mathbf{S}^{(1)}$ and $\mathbf{S}^{(2)}$ represent body forces, e.g., polarization currents

$$\mathbf{S}^{(1)} = \begin{pmatrix} -\epsilon_r(\sigma_x + \sigma_y)E_z + P^m \\ -\mu_r(\sigma_y - \sigma_x)H_x + Q_x^m \\ -\mu_r(\sigma_x - \sigma_y)H_y + Q_y^m \end{pmatrix} \quad (11)$$

$$\mathbf{S}^{(2)} = \begin{pmatrix} -\epsilon_r \sigma_x \sigma_y E_z \\ -\sigma_x Q_x^m + \mu_r \sigma_x (\sigma_y - \sigma_x) H_x \\ -\sigma_y Q_y^m + \mu_r \sigma_y (\sigma_x - \sigma_y) H_y \end{pmatrix}. \quad (12)$$

Similar equations can be derived for the TE case and will not be repeated here.

III. DISCONTINUOUS GALERKIN TIME DOMAIN METHOD

To solve (6) in general geometries, the physical domain Ω under consideration is divided into nonoverlapping quadrilateral and/or triangular elements, denoted by K . Each physical element K is then mapped by an isoparametric transformation [16] onto a reference element I , either a reference square $[-1, 1]^2$ or a reference triangle $\{(x, y) | 0 \leq x, y \leq 1, 0 \leq x + y \leq 1\}$.

Let \mathcal{T}_h be a discretization of the solution domain Ω ; ϵ_r and μ_r are assumed constant on each element for each element $K \in \mathcal{T}_h$. We denote a finite dimensional space of smooth functions (polynomials for DGTD methods) defined on the element K by $\mathcal{P}(K)$, which will be used to approximate the variable \mathbf{U} . We define

$$V_h := \{v \in L^1(\Omega) \mid v|_K \in \mathcal{P}(K) \quad \forall K \in \mathcal{T}_h\} \quad (13)$$

and

$$V_h^6 := \underbrace{V_h \times V_h \times \cdots \times V_h}_6. \quad (14)$$

The DGTD space discretization of the hyperbolic system (7) and (8) can be obtained as follows: Find $\mathbf{U} \in V_h^6$ such that for all $v_h \in V_h$

$$\int_K \left(\frac{\partial \mathbf{U}^{(1)}}{\partial t} v_h - \mathbf{S}^{(1)} v_h - \mathbb{A} \mathbf{U}^{(1)} \cdot \nabla v_h \right) dx + \int_{\partial K} \mathbf{h}_K \left(\mathbf{U}^{(1),-}, \mathbf{U}^{(1),+} \right) \cdot \hat{\mathbf{n}}_K v_h ds = 0 \quad (15)$$

$$\int_K \left(\frac{\partial \mathbf{U}^{(2)}}{\partial t} v_h - \mathbf{S}^{(2)} v_h \right) dx = 0 \quad (16)$$

where $\hat{\mathbf{n}}_K = (n_x, n_y)$ is the outward unit normal to ∂K , and $\mathbf{U}^{(1),-}$ and $\mathbf{U}^{(1),+}$ are defined as

$$\mathbf{U}^{(1),\pm}(\mathbf{x}) = \lim_{\delta \rightarrow 0^+} \mathbf{U}^{(1)}(\mathbf{x} \pm \delta \hat{\mathbf{n}}_k)$$

as \mathbf{U} is, in general, discontinuous across ∂K , the numerical flux $\mathbf{h}_K(\mathbf{U}^{(1),-}, \mathbf{U}^{(1),+})$ is an approximation to $\hat{\mathbf{n}}_K \cdot \mathbb{A} \mathbf{U}^{(1)}|_{\partial K}$ on the faces of the element K , and should satisfy the following consistent condition

$$\mathbf{h}_K \left(\mathbf{U}^{(1)}, \mathbf{U}^{(1)} \right) = \hat{\mathbf{n}}_K \cdot \mathbb{A} \mathbf{U}^{(1)}|_{\partial K}. \quad (17)$$

We can obtain $\mathbf{h}_K(\mathbf{U}^{(1),-}, \mathbf{U}^{(1),+})$ by solving a local Riemann problem. In [11] and [17], the Riemann problem for Maxwell's equations is discussed in detail, which gives a numerical flux $\mathbf{h}_K(\mathbf{U}^{(1),-}, \mathbf{U}^{(1),+})$ for the 3-D Maxwell's equations as

$$\mathbf{h}_K = \begin{pmatrix} -\hat{\mathbf{n}}_K \times \frac{(Z\mathbf{H} + \hat{\mathbf{n}}_K \times \mathbf{E})^- + (Z\mathbf{H} - \hat{\mathbf{n}}_K \times \mathbf{E})^+}{Z^- + Z^+} \\ \hat{\mathbf{n}}_K \times \frac{(Y\mathbf{E} - \hat{\mathbf{n}}_K \times \mathbf{H})^- + (Y\mathbf{E} + \hat{\mathbf{n}}_K \times \mathbf{H})^+}{Y^- + Y^+} \end{pmatrix} \quad (18)$$

where Z^\pm and Y^\pm are the local impedance and admittance, respectively, and are defined as

$$Z^\pm = \frac{1}{Y^\pm} = \sqrt{\frac{\mu_r^\pm}{\epsilon_r^\pm}}.$$

For the TM case, from (18), the numerical flux is reduced to

$$\mathbf{h}_K \left(\mathbf{U}^{(1),-}, \mathbf{U}^{(1),+} \right) = \begin{pmatrix} -\frac{[Z(n_x H_y - n_y H_x) - E_z]^- + [Z(n_x H_y - n_y H_x) + E_z]^+}{Z^- + Z^+} \\ n_y \frac{[Y E_z - (n_x H_y - n_y H_x)]^- + [Y E_z + (n_x H_y - n_y H_x)]^+}{Y^- + Y^+} \\ -n_x \frac{[Y E_z - (n_x H_y - n_y H_x)]^- + [Y E_z + (n_x H_y - n_y H_x)]^+}{Y^- + Y^+} \end{pmatrix} \quad (19)$$

where $\mathbf{U}^{(1)} = (\epsilon_r E_z, \mu_r H_x, \mu_r H_y)^T$, while the numerical flux for TE case is

$$\mathbf{h}_K \left(\mathbf{U}^{(1),-}, \mathbf{U}^{(1),+} \right) = \begin{pmatrix} \frac{[Y(n_x E_y - n_y E_x) + H_z]^- + [Y(n_x E_y - n_y E_x) - H_z]^+}{Y^- + Y^+} \\ -n_y \frac{[ZH_z + (n_x E_y - n_y E_x)]^- + [ZH_z - (n_x E_y - n_y E_x)]^+}{Z^- + Z^+} \\ n_x \frac{[ZH_z + (n_x E_y - n_y E_x)]^- + [ZH_z - (n_x E_y - n_y E_x)]^+}{Z^- + Z^+} \end{pmatrix} \quad (20)$$

where $\mathbf{U}^{(1)} = (\mu_r H_z, \epsilon_r E_x, \epsilon_r E_y)^T$.

A. Basis Function Space $\mathcal{P}(K)$

By constructing a set of basis functions on a standard reference element I , we can obtain a basis function space $\mathcal{P}(K)$ on the physical element K using a mapping Ψ between I and K . For example, we can define a set of basis functions for the standard rectangular element

$$\text{span} \{L_i(\xi)L_j(\eta); i, j \geq 0; i + j \leq n\} = \text{span} \{\phi_j\}_{j=1}^N \quad (21)$$

where $L_i(\cdot)$ is the Legendre polynomial of order i , and $N = (n+2)(n+1)/2$.

A set of basis functions on the standard reference triangle element I can be defined as

$$P_n^2 = \text{span} \{\xi^i \eta^j; i, j \geq 0; i + j \leq n\} = \text{span} \{\phi_j\}_{j=1}^N \quad (22)$$

where n is the maximum order of the polynomial, and $N = (n+2)(n+1)/2$. Dubiner orthogonal polynomial basis functions are a good choice when higher order basis ($n > 7$) is used in triangular elements; they can provide well-conditioned mass matrices defined in (34) and yield exponential convergence even for discontinuous fields [12].

The set of basis functions on each physical element K is obtained by the mapping Ψ as

$$\text{span} \{\phi_j(\xi(x, y), \eta(x, y)); 1 \leq j \leq N\} \quad (23)$$

where $(\xi, \eta) = \Psi^{-1}(x, y)$.

B. Space Discretization

Expand the electric field E_z and magnetic fields H_x and H_y in terms of the basis functions $\phi_j(\mathbf{x})$

$$E_{z,N}(\mathbf{x}, t) = \sum_{j=1}^N E_{z,j} \phi_j(\mathbf{x}) \quad (24)$$

$$H_{s,N}(\mathbf{x}, t) = \sum_{j=1}^N H_{s,j} \phi_j(\mathbf{x}), \quad s = x, y \quad (25)$$

where $E_{z,j}$, $H_{x,j}$, and $H_{y,j}$ are functions of time and $\phi_j(\mathbf{x})$ is the j th basis function. We also project $\mathbf{U}^{(2)}$ to the function space expanded by the basis functions

$$P^{m,N}(\mathbf{x}, t) = \sum_{j=1}^N P_{m,j} \phi_j(\mathbf{x}) \quad (26)$$

$$Q_s^{m,N}(\mathbf{x}, t) = \sum_{j=1}^N Q_{s,m,j} \phi_j(\mathbf{x}), \quad s = x, y. \quad (27)$$

On each element K setting $v_h = \phi_j(\mathbf{x})$ in (15) and (16), a system of ordinary differential equations (ODEs) will be obtained for the expansion coefficients (24)–(27).

We define the unknown vectors on each element K

$$\begin{aligned} \mathbf{E}^z &= (E_{z,1}, E_{z,2}, \dots, E_{z,N})^T \\ \mathbf{H}^s &= (H_{s,1}, H_{s,2}, \dots, H_{s,N})^T, \quad s = x, y \\ \mathbf{P}^m &= (P_{m,1}, P_{m,2}, \dots, P_{m,N})^T \\ \mathbf{Q}_s^m &= (Q_{s,m,1}, Q_{s,m,2}, \dots, Q_{s,m,N})^T, \quad s = x, y \end{aligned}$$

and also the basis function vector

$$\boldsymbol{\phi} = (\phi_1, \phi_2, \dots, \phi_N)^T.$$

Assuming ϵ_r , μ_r , σ_x , σ_y be constant on each element K , we can obtain the following ODEs for the unknown vectors while Gauss quadrature formulations are used to evaluate the integration in (15) and (16)

$$\begin{aligned} \frac{d\mathbf{E}^z}{dt} &= -(\epsilon_r M)^{-1} M^x \mathbf{H}^y + (\epsilon_r M)^{-1} M^y \mathbf{H}^x - (\epsilon_r M)^{-1} \\ &\times \int_{\partial D} h_D^{E_z} \left(\mathbf{U}_N^{(1),-}, \mathbf{U}_N^{(1),+} \right) \boldsymbol{\phi}(x) ds + \frac{1}{\epsilon_r} \mathbf{S}_N^{E_z} \end{aligned} \quad (28)$$

where

$$\begin{aligned} \mathbf{S}_N^{E_z} &= \left(S_1^{E_z}, S_2^{E_z}, \dots, S_N^{E_z} \right)^T \\ S_j^{E_z} &= -\epsilon_r (\sigma_x + \sigma_y) E_{z,j} + P_{m,j} \\ \frac{d\mathbf{H}^x}{dt} &= (\mu_r M)^{-1} M^y \mathbf{E}^z - (\mu_r M)^{-1} \\ &\times \int_{\partial D} h_D^{H_x} \left(\mathbf{U}_N^{(1),-}, \mathbf{U}_N^{(1),+} \right) \boldsymbol{\phi}(x) ds + \frac{1}{\mu_r} \mathbf{S}_N^{H_x} \end{aligned} \quad (29)$$

where

$$\begin{aligned} \mathbf{S}_N^{H_x} &= \left(S_1^{H_x}, S_2^{H_x}, \dots, S_N^{H_x} \right)^T \\ S_j^{H_x} &= -\mu_r (\sigma_y - \sigma_x) H_{x,j} + Q_{x,m,j} \\ \frac{d\mathbf{H}^y}{dt} &= -(\mu_r M)^{-1} M^x \mathbf{E}^z - (\mu_r M)^{-1} \\ &\times \int_{\partial D} h_D^{H_y} \left(\mathbf{U}_N^{(1),-}, \mathbf{U}_N^{(1),+} \right) \boldsymbol{\phi}(x) ds + \frac{1}{\mu_r} \mathbf{S}_N^{H_y} \end{aligned} \quad (30)$$

where

$$\begin{aligned} \mathbf{S}_N^{H_y} &= \left(S_1^{H_y}, S_2^{H_y}, \dots, S_N^{H_y} \right)^T \\ S_j^{H_y} &= -\mu_r (\sigma_x - \sigma_y) H_{y,j} + Q_{y,m,j}. \end{aligned}$$

Furthermore

$$\frac{dP_{m,j}}{dt} = -\epsilon_r \sigma_x \sigma_y E_{z,j} \quad (31)$$

$$\frac{dQ_{x,m,j}}{dt} = -\sigma_x Q_{x,m,j} + \mu_r \sigma_x (\sigma_y - \sigma_x) H_{x,j} \quad (32)$$

$$\frac{dQ_{y,m,j}}{dt} = -\sigma_y Q_{y,m,j} + \mu_r \sigma_y (\sigma_x - \sigma_y) H_{y,j}. \quad (33)$$

Here, M_{ij} is the local mass matrix defined as

$$M_{ij} = \int_D \phi_i(\mathbf{x}) \phi_j(\mathbf{x}) d\mathbf{x} \quad (34)$$

and M_{ij}^x and M_{ij}^y are two local stiffness matrices defined as

$$M_{ij}^x = \int_D \frac{\partial \phi_i(\mathbf{x})}{\partial x} \phi_j(\mathbf{x}) d\mathbf{x}$$

$$M_{ij}^y = \int_D \frac{\partial \phi_i(\mathbf{x})}{\partial y} \phi_j(\mathbf{x}) d\mathbf{x}.$$

IV. NUMERICAL RESULTS

Simulation Geometry and Parameters: A typical geometry of a waveguide-coupled microring resonator is shown in Fig. 1. A mode in the form of continuous wave or an impulse is excited at the left end of waveguide WG1, and waveguides WG1 and WG2 serve as evanescent wave input and output couplers. For all numerical examples, the reference length $L = 1 \mu\text{m}$. For the single-ring case, we set the center of the ring as the origin of the coordinate system. The ring's outer radius is $R = 1.7 \mu\text{m}$, the width of WG1, WG2 and the ring is $0.2 \mu\text{m}$, the separation of the ring and waveguide is denoted as g which can be adjusted for different examples, while the separation of the waveguide and UPML region $h = 0.2 \mu\text{m}$. The width of the physical region is $4 \mu\text{m}$, and the height of the physical region is $4.2 \mu\text{m}$ plus $2g$ (g again is the separation of waveguide and microring). For the case of two microrings, we have used the

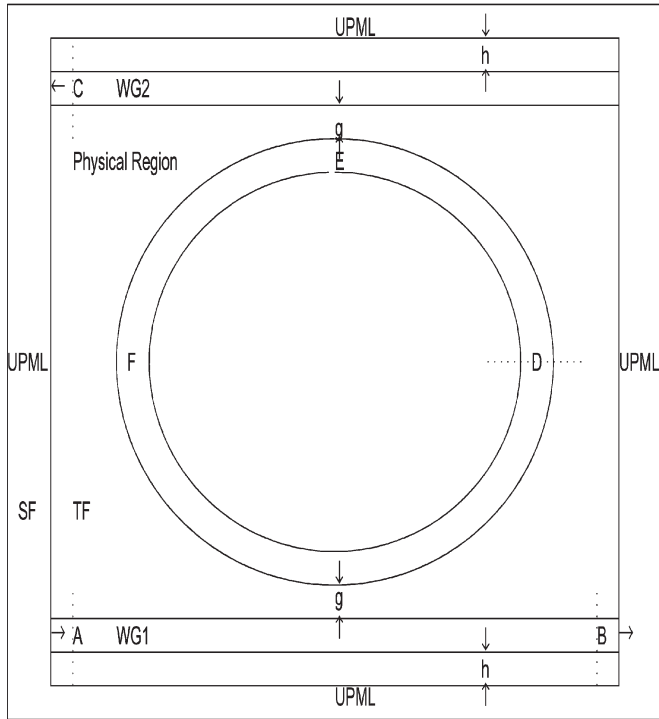


Fig. 1. Schematic of a microresonator (a microring coupled to two straight waveguides) and UPML layer.

same parameters as the single-ring case except that we put the origin of the coordinate system at the middle point of the center-to-center line, and the separation of the ring and waveguide and the gap between the rings is $g = 0.1 \mu\text{m}$.

The ring and the waveguide have the same index value $n = 3.0$, surrounded by air ($n_0 = 1.0$). We will use sinusoidal excitation to study numerical convergence and pulse excitation to get coupling efficiency and transmittance.

We use a five-cell UPML (with a total thickness of 2) for $\Delta x = 0.4$, a five-cell UPML (with a total thickness of 1) for $\Delta x = 0.2$, a 10-cell UPML (of thickness 1) for $\Delta x = 0.1$, and a 20-cell UPML (of thickness 1) for $\Delta x = 0.05$. The UPML parameters are $R(0) = e^{-16}$, $m = 3$ for a 10-cell and a 20-cell UPML, and $R(0) = e^{-8}$, $m = 3$ for a five-cell UPML. We use a freeware software Easymesh [20] to discretize the physical region with unstructured triangles and the UPML region with rectangles. Mesh conformity is enforced along the UPML interface. Δx represents the maximum dimension of all mesh elements, except the examples of studying convergence rate, and Δx is set to 0.1.

The total field in the physical region and the scattered field in the UPML region are calculated using total-field/scattered-field (TF/SF) technique discussed below. A fourth-order Runge—Kutta method is employed for the time integration of the ODE systems (28)–(33); $\Delta t = 0.008$ for $\Delta x = 0.2$ and $\Delta x = 0.4$, $\Delta t = 0.004$ for $\Delta x = 0.1$, and $\Delta t = 0.002$ for $\Delta x = 0.05$, and the time step is taken heuristically to be

$$\Delta t = \text{CFL} \min_{\Omega} \sqrt{\epsilon_r \mu_r} l$$

l is the minimum length of the sides, and CFL typically takes the value of $1/(2n + 1)$; here, n is the order of basis functions,

and $n = 4$ in all the examples. More rigorous criteria for the selection of the time steps for unstructured meshes can be found in [19].

Time Interval of Simulations: Time interval $T = 40$ is used to calculate coupling efficiency and $T = 600$ to calculate transmittance of the single-ring case. For the two-ring case, time interval $T = 60$ is used for calculating coupling efficiency and $T = 1000$ for calculating transmittance. Finally, for the steady state of an on-resonance or off-resonance, the time interval $T = 200$ is used for the single-ring case and time interval $T = 400$ for the two-ring case.

Memory Requirements: The memory requirement for DGTD is N , where N is the degree of freedom of the numerical solution. In the one-ring case with $\Delta x = 0.1$ and four-order basis functions, N is around 300 000. The memory requirement for FDTD for a 3-D computation is [15]

$$6N_x N_y N_z + 8N_{\text{UPML}}(N_x N_y + N_y N_z + N_z N_x) - 16N_{\text{UPML}}(N_x + N_y + N_z) + (24N_{\text{UPML}})^2$$

where N_{UPML} is the thickness of the UPML, and N_i , $i = x, y, z$, is the number of mesh point in each dimension. For a 2-D TE case or a 2-D TM case, the memory requirement for the FDTD is about 15 000 with $\Delta x = 0.1$ and a ten-cell UPML.

Number of Floating Point Operations: To compute the right-hand side in (28)–(30) for the DGTD, it takes about 5500 floating point operations with four-order basis functions and 900 floating point operations with two-order basis functions. While in the FDTD, the number of floating point operations needed for space discretization is around 17 for each mesh point. In the one-ring case with $\Delta x = 0.1$ and four-order basis functions, the wall clock time for the DGTD is approximately 150 min for a simulation time interval $T = 50$ using eight nodes on LSSC-II [21].

A. Numerical Fluxes and Input Sources

1) TF/SF Technique in DGTD Methods: The TF/SF formulation is based on the linearity of Maxwell’s equations and widely used in FDTD modeling [15]. It permits modeling of long-duration pulsed or sinusoidal illuminations for arbitrary plane-wave propagation directions. We will also use this formulation in the DGTD by changing the flux (18) on the interface between physical media and UPML regions. Suppose the field $\mathbf{U}^{(1),-}$ is the value on the element being considered and $\mathbf{U}^{(1),+}$ is the value on a neighboring element. The stored $\mathbf{U}^{(1)}$ in the physical media is the total field, and in the UPML region is the scattered field. If the first element is in the physical media and the neighboring element is in the UPML, the flux (18) will be modified to be

$$\mathbf{h}_K = \begin{pmatrix} -\hat{\mathbf{n}}_K \times \frac{[Z\mathbf{H} + \hat{\mathbf{n}}_K \times \mathbf{E}]^- + [Z(\mathbf{H} + \mathbf{H}_{\text{inc}}) - \hat{\mathbf{n}}_K \times (\mathbf{E} + \mathbf{E}_{\text{inc}})]^+}{Z^- + Z^+} \\ \hat{\mathbf{n}}_K \times \frac{[Y\mathbf{E} - \hat{\mathbf{n}}_K \times \mathbf{H}]^- + [Y(\mathbf{E} + \mathbf{E}_{\text{inc}}) + \hat{\mathbf{n}}_K \times (\mathbf{H} + \mathbf{H}_{\text{inc}})]^+}{Y^- + Y^+} \end{pmatrix}. \quad (35)$$

Otherwise, the flux (18) changes to

$$\mathbf{h}_K = \begin{pmatrix} -\hat{\mathbf{n}}_K \times \frac{[Z\mathbf{H} + \hat{\mathbf{n}}_K \times \mathbf{E}]^- + [Z(\mathbf{H} - \mathbf{H}_{\text{inc}}) - \hat{\mathbf{n}}_K \times (\mathbf{E} - \mathbf{E}_{\text{inc}})]^+}{Z^- + Z^+} \\ \hat{\mathbf{n}}_K \times \frac{[Y\mathbf{E} - \hat{\mathbf{n}}_K \times \mathbf{H}]^- + [Y(\mathbf{E} - \mathbf{E}_{\text{inc}}) + \hat{\mathbf{n}}_K \times (\mathbf{H} - \mathbf{H}_{\text{inc}})]^+}{Y^- + Y^+} \end{pmatrix} \quad (36)$$

where \mathbf{E}_{inc} and \mathbf{H}_{inc} are the values of the incident-wave fields, assumed to be known at all points on the face between physical domain and UPML at all time steps.

2) *Sourcing Specific Waveguide Modes:* We can source a propagating TE (TM) mode of a dielectric slab by specifying the electromagnetic field distribution along a one-dimensional (1-D) transverse cross section of the waveguide. In the case of a sinusoidal excitation, the distribution of desired mode can be obtained by solving an equation for the transverse propagation and the decay constants [18].

In the case of a pulsed source, such as a Gaussian pulse modulating a carrier wave, a method called “bootstrapping” is described in [15]. Here, we obtain an accurate Gaussian pulse inside dielectric slab waveguide by the following steps.

- 1) Assume that the time dependence for the pulse is

$$f(t) = \exp[i\omega_c(t - t_0)] \exp\left[-\left(\frac{t - t_0}{t_{\text{Decay}}}\right)^2\right]$$

where the ω_c is a selected central frequency.

- 2) Take the Fourier transform of $f(t)$

$$\hat{f}(\omega) = \frac{t_{\text{Decay}}}{\sqrt{2}} \exp\left(-\frac{(\omega_c - \omega)^2 t_{\text{Decay}}^2}{4}\right) \exp(-it_0\omega).$$

- 3) Set

$$f(x, y, t) = \frac{1}{\sqrt{2\pi}} \int F(x, y, \omega) \hat{f}(\omega) \exp(i\omega t) d\omega$$

where $F(x, y, \omega)$ is the distribution of desired mode in the case of sinusoidal excitation mentioned above. $f(x, y, t)$ so defined will satisfy the Maxwell’s equations inside a dielectric slab waveguide and contains a range of frequencies around ω_c .

B. Waveguide-Coupled Microring Resonators

Coupling Efficiency and Transmittance: The coupling efficiency between the input/output waveguides and microring is computed as in [15]. Coupling efficiency gives an estimation of how much energy is transferred from waveguide to microring. The coupling efficiency is defined as the ratio between the power at the cross section of the microring at location $D(y = 0 \mu\text{m})$ in Fig. 1 and that at the cross section of the input waveguide at location $A(x = -1.85 \mu\text{m})$ in Fig. 1. However, the power at location D is computed using the fields recorded for the duration when the whole pulse passes the cross section at D for the first time along the microring. We then compute the discrete Fourier transform (DFT) of the time-dependent fields and integrate the Poynting power densities across the waveguide cross section to get the power as a function of the frequency. The integration for the power density is done along

a region that is three times bigger than the cross section of the waveguide or microring in order to get an estimated 99% of the full modal power.

Transmittance gives an estimation of how much energy go through original waveguide and how much is transmitted by the microring. The transmittance spectrum at the right port of WG1 is defined as the ratio between the power at the cross section of the waveguide WG1 at location $B(x = 1.85 \mu\text{m})$ in Fig. 1 and that at the cross section of the input waveguide at location $A(x = -1.85 \mu\text{m})$ in Fig. 1. The transmittance spectrum at the left port of WG2 is defined as the ratio between the power at the cross section of the waveguide WG2 at location $C(x = -1.85 \mu\text{m})$ in Fig. 1 and that at the cross section of the input waveguide at location $A(x = -1.85 \mu\text{m})$ in Fig. 1. The difference with computing coupling efficiency is that we need to record the whole process of the pulse movement until the energy in the resonator and the amplitudes of the pulse have sufficiently decayed.

1) *Single-Ring Case:* We will study the numerical convergence of DGTD methods for calculating the coupling efficiency and transmittance between waveguides and a microring resonator. We use a TE sinusoidal excitation with $\omega = 224 \text{ THz}$ in the $g = 0.1 \mu\text{m}$ case. First, we compute with the DGTD method on a fine mesh $\Delta x = 0.05$, and the result denoted by H_z^3 will be used as a reference to measure the numerical convergence. Then, we apply the DGTD method with $\Delta x = 0.2$ and $\Delta x = 0.1$ to obtain solutions H_z^1, H_z^2 , respectively. We record the H_z field at a fixed point in the output port of WG2, which will be a function of time, and define the error in time at that location as

$$\|H_z^i - H_z^j\|_{\text{error}} = \sqrt{\int (H_z^i - H_z^j)^2 dt}, \quad i \neq j. \quad (37)$$

Here, the integration is over a time period when the field becomes steady. The following numerical convergence is obtained:

$$\begin{aligned} \|H_z^1 - H_z^3\|_{\text{error}} &= 2.4724e - 3 \\ \|H_z^2 - H_z^3\|_{\text{error}} &= 9.6631e - 5 \end{aligned}$$

giving a convergence rate Δx^r , where $r = 4.6$.

Considering the same structure and parameters described above, we use a TE Gaussian pulse with central frequency $\omega_c = 224 \text{ THz}$ for excitation, and we compute coupling efficiency with three different meshes mentioned above, defined as $\text{TE}^1(\omega)$, $\text{TE}^2(\omega)$, $\text{TE}^3(\omega)$, respectively. From the L^2 norm error over the frequency concerned (from 200 to 250 THz for this example), we obtain the following numerical convergence in coupling efficiency:

$$\|\text{TE}^1(\omega) - \text{TE}^3(\omega)\|_{L^2} = 4.9594e - 4$$

and

$$\|\text{TE}^2(\omega) - \text{TE}^3(\omega)\|_{L^2} = 4.0459e - 6$$

giving a convergence rate Δx^r , where $r = 6.94$. Fig. 2(a) shows a coupling efficiency of three meshes; the results for

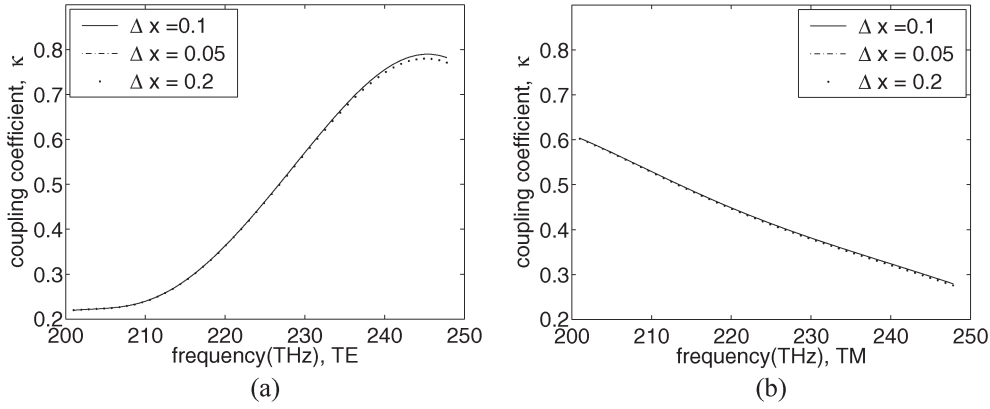


Fig. 2. Coupling efficiency κ as a function of frequency with different meshes for the $g = 0.1 \mu\text{m}$ and $3.4\text{-}\mu\text{m}$ -diameter ring of Fig. 1. (a) TE polarization. (b) TM polarization.

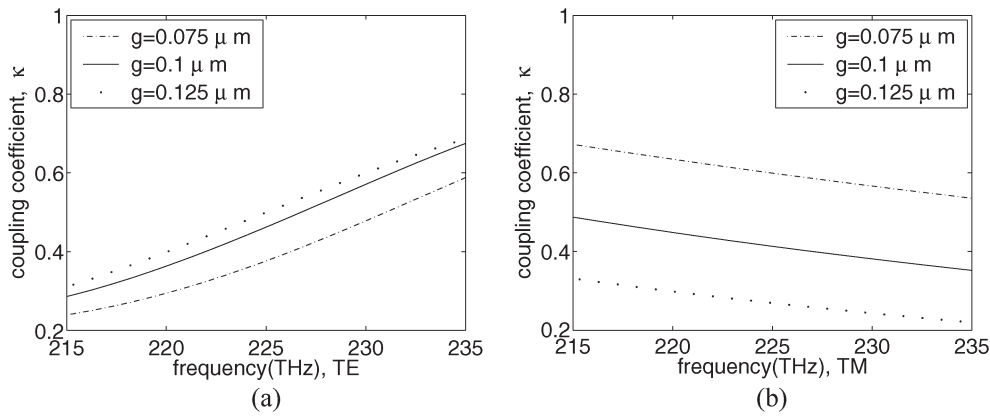


Fig. 3. Coupling efficiency κ as a function of frequency and gap size g for a $3.4\text{-}\mu\text{m}$ -diameter ring of Fig. 1 with $\Delta x = 0.1$. (a) TE polarization. (b) TM polarization.

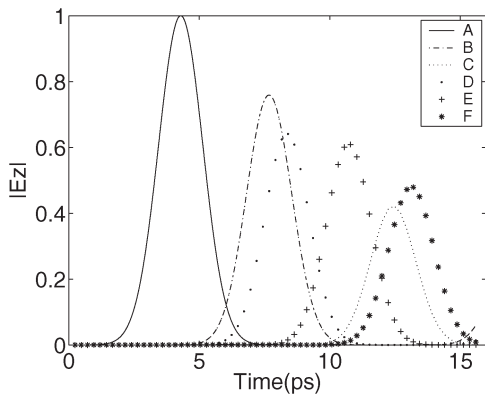


Fig. 4. Time history of pulse at various locations indicated in Fig. 1 when $g = 0.1 \mu\text{m}$ for a $3.4\text{-}\mu\text{m}$ -diameter ring of Fig. 1 with $\Delta x = 0.1$ (TM polarization).

the $\Delta x = 0.05$ case and the $\Delta x = 0.1$ case are hard to distinguish in the plot.

We also consider a TM Gaussian pulse in the same frequency domain, resulting in the following convergence:

$$\|TM^1(\omega) - TM^3(\omega)\|_{L^2} = 4.8728e - 4$$

and

$$\|TM^2(\omega) - TM^3(\omega)\|_{L^2} = 2.3271e - 6$$

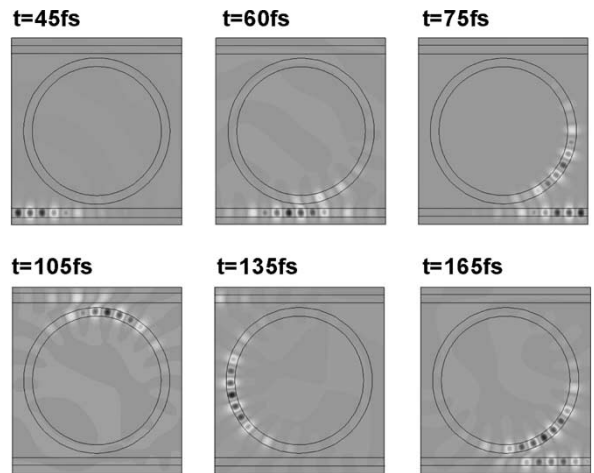


Fig. 5. Visualization of snapshots in time of DGTD-computed E_z field of a pulse circling around a $3.4\text{-}\mu\text{m}$ -diameter ring of Fig. 1 with $\Delta x = 0.1$ and $g = 0.1 \mu\text{m}$ (TM polarization).

with a convergence rate Δx^r , where $r = 8.0$. Again, Fig. 2(b) shows a coupling efficiency of three meshes with result for the $\Delta x = 0.05$ case indistinguishable from that of the $\Delta x = 0.1$ case.

Effect of Gaps Between Waveguides and Microring(s) on Coupling Efficiency and Transmittance: Here, we will

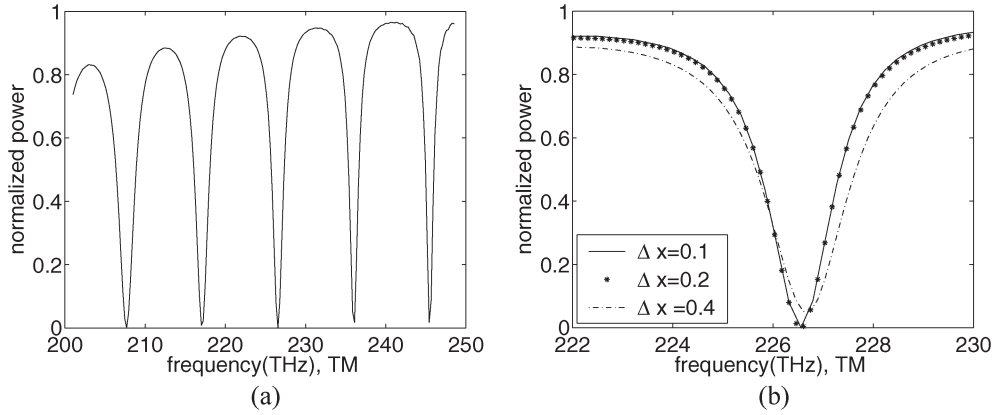


Fig. 6. DGTD-computed transmittance spectrum of the 3.4- μm -diameter ring of Fig. 1 ($g = 0.1 \mu\text{m}$) at the right port of WG1 (TM polarization). (a) Transmittance spectrum with $\Delta x = 0.1$. (b) Comparison with three different meshes.

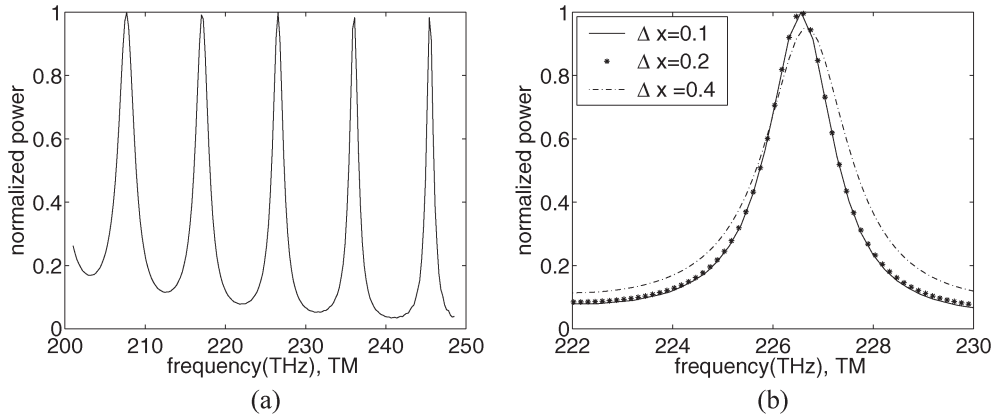


Fig. 7. DGTD-computed transmittance spectrum of the 3.4- μm -diameter ring of Fig. 1 ($g = 0.1 \mu\text{m}$) at the left port of WG2 (TM polarization). (a) Transmittance spectrum with $\Delta x = 0.1$. (b) Comparison with three different meshes.

investigate the effect of the separation between the input/output waveguides on the coupling efficiency and transmittance of the waveguide-microring resonators.

Fig. 3(a) and (b) shows the coupling efficiency of different polarization modes and different separations. Here, we used a mesh $\Delta x = 0.1$ and a Gaussian pulse with central frequency $\omega_c = 224 \text{ THz}$. From the two figures, we observe that TM polarization and TE polarization behave differently as the gap between the waveguides and rings varies.

- 1) For a fixed frequency, as the gap size increases, the coupling efficiency for the TM polarization decreases, while that for the TE polarization increases.
- 2) For a fixed gap size, as the frequency increases, the coupling efficiency for the TM polarization decreases, while that for the TE polarization increases.

The difference of the dependence of the coupling efficiency on the gap for the case of TE and TM could be related to the fact that in the TM case, all fields are continuous, while the electric fields for the TE case are discontinuous across the waveguide/microring boundaries. This fact might cause stronger reflection for the TE case than the TM case. A smaller

gap will feel the effects of reflections more, thus, the inverse dependence of the coupling efficiency on the gap for the TE case.

In Fig. 4, we plot the time history of the normalized $|E|$ at some selected observation points marked as A, B, C, D, E, and F in Fig. 1, which demonstrates the pulse propagation inside the structure. Snapshots at various times of DGTD-computed E_z field (perpendicular to the plane) is shown in Fig. 5 as the pulse couples into the ring and completes one round trip around the ring. The transmittance spectrum at the right port of WG1 is shown in Fig. 6(a), and the transmittance spectrum at the left port of WG2 is shown in Fig. 7(a). We use three different meshes to study transmittance spectrum in Figs. 6(b) and 7(b), which shows the convergence for the location of the resonance frequency. From the transmittance spectrum in Fig. 6(a), we can select an on-resonant frequency $\omega = 226.5587 \text{ THz}$, where the transmittance is at a minimum, and an off-resonant frequency $\omega = 241.3601 \text{ THz}$, where the transmittance is at a maximum. Fig. 8(a) shows the steady-state electric field for a continuous wave (CW) excitation at the on-resonant frequency, while Fig. 8(b) shows the steady-state electric field for a CW excitation at the off-resonant frequency.

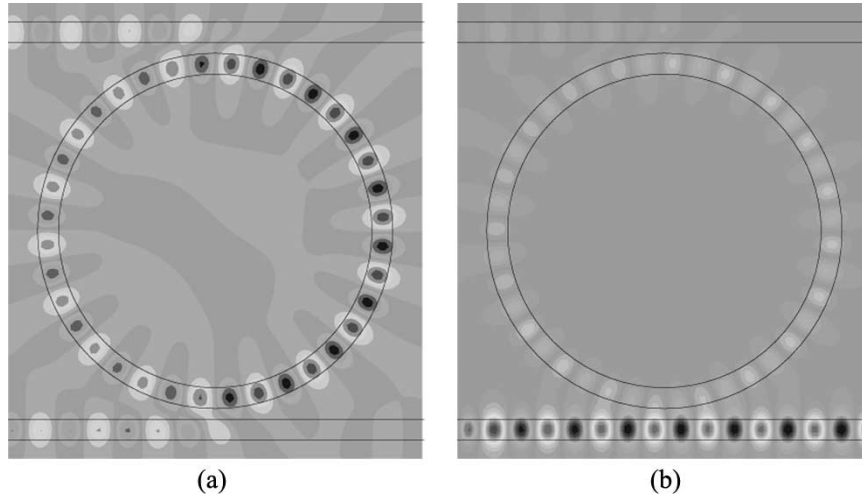


Fig. 8. Visualization of DGTD-computed steady-state E_z field for the 3.4- μm -diameter ring of Fig. 1 with $\Delta x = 0.1$ and $g = 0.1 \mu\text{m}$ (TM polarization). Here, a single-frequency CW excitation is applied at port A of WG1. (a) On-resonant frequency 226.5587 THz. (b) Off-resonant frequency 241.3601 THz.

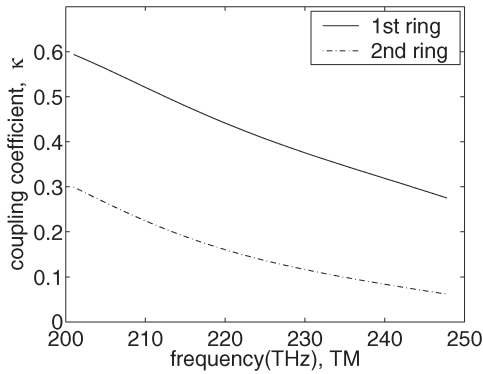


Fig. 9. Coupling efficiency κ as a function of frequency when gap size $g = 0.1 \mu\text{m}$ and $\Delta x = 0.1$ for a 3.4- μm -diameter two-ring case (TM polarization).

2) *Two-Ring Case:* In Fig. 9, we plot the coupling efficiency of a two-ring case. The process of computing the coupling efficiency is similar to that of the single-ring case. The sampling of the input is done along the cross section at the location $A(x = -1.85 \mu\text{m}, y = -3.65 \mu\text{m})$ in Fig. 10(a). For the coupling coefficient of the first ring, the sampling of the field is along the cross section at location $D(x = 1.6 \mu\text{m}, y = -1.75 \mu\text{m})$ in Fig. 10(a), while for the coupling efficiency of the second ring, the sampling is at the cross section at location $E(x = -1.6 \mu\text{m}, y = 1.75 \mu\text{m})$ in Fig. 10(a). The size of the cross section is the same as the single-ring case.

The transmittance spectrum at the right port of WG1 is defined as the ratio between the power at the cross section of the waveguide WG1 at location $B(x = 1.85 \mu\text{m}, y = -3.65 \mu\text{m})$ in Fig. 10(a) and that at the cross section of the input waveguide at location $A(x = -1.85 \mu\text{m}, y = -3.65 \mu\text{m})$ in Fig. 10(a). The transmittance spectrum at the right port of WG2 is defined as the ratio between the power at the cross section of the waveguide WG2 at location $C(x = 1.85 \mu\text{m}, y = 3.65 \mu\text{m})$ in Fig. 10(a) and that at the cross section of the input waveguide at location $A(x = -1.85 \mu\text{m}, y = -3.65 \mu\text{m})$ in Fig. 10(a).

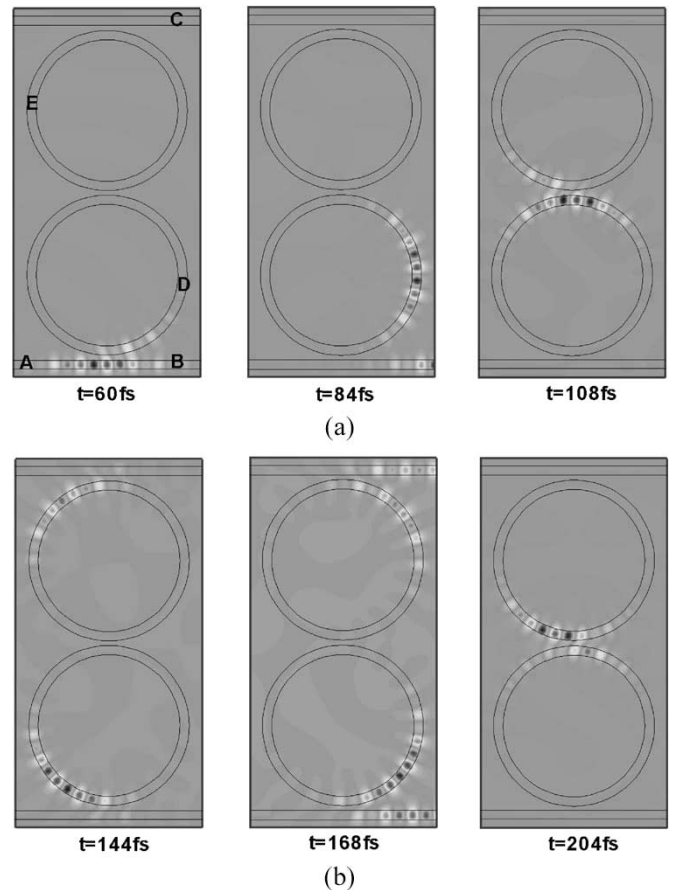


Fig. 10. Visualization of snapshots in time of DGTD-computed E_z field of a pulse travelling around a 3.4- μm -diameter two-ring case when gap size $g = 0.1 \mu\text{m}$ and $\Delta x = 0.1$ (TM polarization).

Fig. 10(a) and (b) gives snapshots in time of E_z field as the pulse propagates. Fig. 11 shows transmittance spectrum at the right port of WG1, while Fig. 12 shows transmittance spectrum at the right port of WG2. Single resonance in the single-ring case split into two resonances in the two-ring case due to the

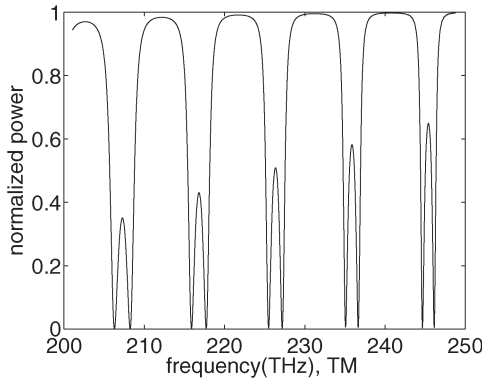


Fig. 11. DGTD-computed transmittance spectrum of the 3.4- μm -diameter two-ring case at the right port of WG1 when gap size $g = 0.1 \mu\text{m}$ and $\Delta x = 0.1$ (TM polarization).

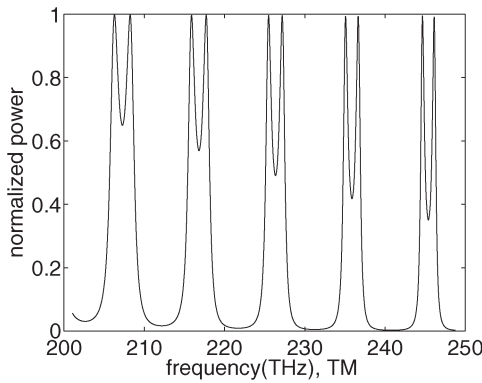
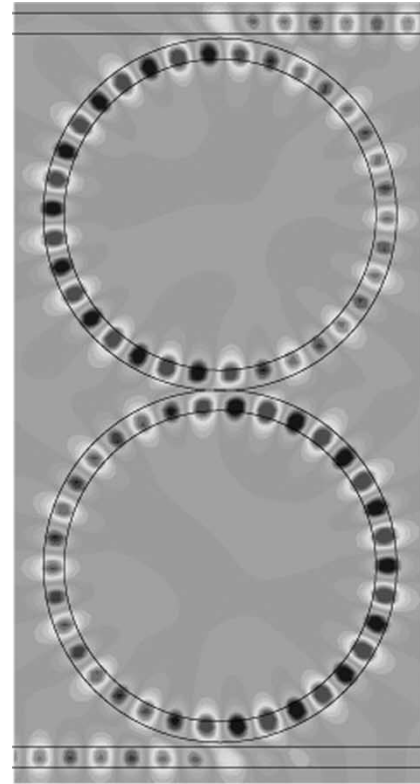


Fig. 12. DGTD-computed transmittance spectrum of the 3.4- μm -diameter two-ring case at the right port of WG2 when gap size $g = 0.1 \mu\text{m}$ and $\Delta x = 0.1$ (TM polarization).

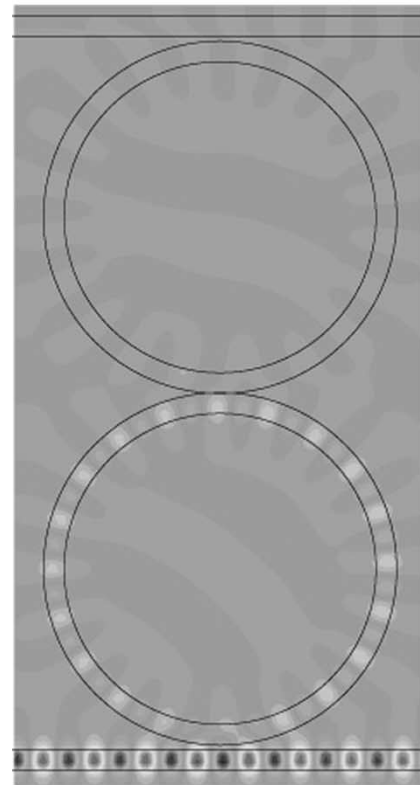
interaction of the rings. In [13], we have given an analysis of the interaction of metal nanowires. There is only one plasmon resonance frequency in one metal cylinder nanowire, while when several metal cylinders are brought together close enough, the resonance pattern becomes more complex because of plasmon interactions. The phenomena here can be interpreted similarly. Fig. 13(a) shows the steady-state electric field pattern for CW excitation at an on-resonance signal $\omega = 217.7255 \text{ THz}$; Fig. 13(b) shows the steady-state electric field pattern for a CW excitation at an off-resonance signal $\omega = 248.6653 \text{ THz}$.

V. CONCLUSION

The high-order accuracy of high-order discontinuous Galerkin time domain (DGTd) methods for the calculation of the coupling efficiency and transmittance of waveguide-coupled microring resonators has been demonstrated. If high-order accuracy and phase information of the signals are required, the DGTd method will be superior to the popular Yee’s scheme finite difference time domain (FDTD) method. As the DGTd is based on a finite element type mesh, more storage and number of floating point operations per mesh point will be required. Further work will be needed to treat real three-dimensional (3-D) microring resonators.



(a)



(b)

Fig. 13. Visualization of DGTD-computed steady-state E_z field for the 3.4- μm -diameter two-ring case when gap size $g = 0.1 \mu\text{m}$ and $\Delta x = 0.1$ (TM polarization). Here, a single-frequency CW excitation is applied at port A of WG1. (a) On-resonant frequency 217.7255 THz. (b) Off-resonant frequency 248.6653 THz.

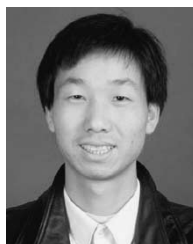
REFERENCES

- [1] M. L. Gorodetsky, A. A. Savchenkov, and V. S. Ilchenko, "Ultimate Q of optical microsphere resonators," *Opt. Lett.*, vol. 21, no. 7, pp. 453–455, 1996.
- [2] K. Oda, S. Suzuki, H. Takahashi, and H. Toba, "An optical FDM distribution experiment using a high finesse waveguide-type double ring resonator," *IEEE Photon. Technol. Lett.*, vol. 6, no. 8, pp. 1031–1034, Aug. 1994.
- [3] R. Orta, P. Savi, R. Tascone, and D. Trincherro, "Synthesis of multiple-ring-resonator filters for optical systems," *IEEE Photon. Technol. Lett.*, vol. 7, no. 12, pp. 1447–1449, Dec. 1995.
- [4] B. E. Little, S. T. Chu, H. A. Haus, J. Foresi, and J. P. Laine, "Microring resonator channel dropping filters," *J. Lightw. Technol.*, vol. 15, no. 6, pp. 998–1005, Jun. 1997.
- [5] A. Yariv, "Universal relations for coupling of optical power between microresonators and dielectric waveguides," *Electron. Lett.*, vol. 36, no. 4, pp. 321–322, 2000.
- [6] M. K. Chin and S. T. Ho, "Design and modeling of waveguide coupled single mode microring resonator," *J. Lightw. Technol.*, vol. 16, no. 8, pp. 1433–1446, Aug. 1998.
- [7] H. A. Haus, W. P. Huang, S. Kawakami, and N. A. Whitaker, "Coupled-mode theory of optical waveguides," *J. Lightw. Technol.*, vol. LT-5, no. 1, pp. 16–23, Jun. 1987.
- [8] S. C. Hagness, D. Rafizadeh, S. T. Ho, and A. Taflove, "FDTD microcavity simulations: Design and experimental realization of waveguide-coupled single-mode ring and whispering-gallery-mode disk resonator," *J. Lightw. Technol.*, vol. 15, no. 11, pp. 2154–2165, Nov. 1997.
- [9] B.-J. Li and P.-L. Liu, "Numerical analysis of the whispering gallery modes by finite difference time domain methods," *IEEE J. Quantum Electron.*, vol. 32, no. 9, pp. 1583–1587, Sep. 1996.
- [10] J. Krupka, D. Cros, M. Aubourg, and P. Guillon, "Study of whispering gallery modes in anisotropic single-crystal dielectric resonators," *IEEE Trans. Microw. Theory Tech.*, vol. 42, no. 1, pp. 56–61, Jan. 1994.
- [11] T. Lu, P. Zhang, and W. Cai, "Discontinuous Galerkin methods for dispersive and lossy Maxwell's equations," *J. Comput. Phys.*, vol. 200, no. 2, pp. 549–580, 2004.
- [12] S. Z. Deng and W. Cai, "Discontinuous spectral element method modeling of optical coupling by whispering gallery modes between microcylinders," *J. Opt. Soc. Amer. A*, vol. 22, no. 5, pp. 952–960, 2005.
- [13] X. Ji, W. Cai, and P. Zhang, "High order (DGTD) simulation of plasmon resonant coupling of metal nanowires," *Opt. Express*, 2005. submitted for publication.
- [14] B. Cockburn, S. Hou, and C.-W. Shu, "Tvb Runge—Kutta local projection discontinuous Galerkin finite element method for conservation laws iv: The multidimensional case," *Math. Comput.*, vol. 54, no. 190, pp. 545–581, 1990.
- [15] A. Taflove and S. C. Hagness, *Computational Electromagnetics: The Finite-Difference Time-Domain Method*, 2nd ed. Boston, MA: Artech House, 2000.
- [16] B. Szabo and I. Babuska, *Finite Element Analysis*. New York: Wiley, 1991.
- [17] A. H. Mohammadian, V. Shankar, and W. F. Hall, "Computation of electromagnetic scattering and radiation using a time-domain finite-volume discretization procedure," *Comput. Phys. Commun.*, vol. 68, no. 1–3, pp. 175–196, 1991.
- [18] R. E. Collin, *Field Theory of Guided Waves*, 2nd ed. New York: Wiley-IEEE Press, 1990.
- [19] T. Warburton, L. Pavarino, and J. S. Hesteven, "A pseudospectral scheme for incompressible Navier Stokes using unstructured nodal element," *J. Comput. Phys.*, vol. 164, no. 1, pp. 1–21, 2000.
- [20] [Online]. Available: <http://www-dinma.univ.trieste.it/nirftc/research/easymesh>
- [21] [Online]. Available: <http://lssc/Manual/lssc2man.txt>



Xia Ji received the B.S. degree in computational mathematics from Peking University, Beijing, China, in 2001. She is currently working toward the Ph.D. degree in computational mathematics also in Peking University.

Her current research interests include computational electromagnetics and the study of plasmon.



Tiao Lu received the B.S. and Ph.D. degrees in computational mathematics from Peking University, Beijing, China, in 1999 and 2004, respectively.

His current research interests include computational electromagnetics and the analysis of the wave propagation in inhomogeneous media.



Wei Cai (S'99–M'00–SM'01) received the Ph.D. degree in applied mathematics from Brown University, Providence, RI, in 1989.

He joined the Department of Mathematics of the University of North Carolina at Charlotte in 1989 as an Assistant Professor and later became an Associate Professor in 1995. During 1995–1996, he joined the Department of Mathematics of the University of California at Santa Barbara as an Assistant Professor and later became an Associate Professor. Since 1999, he has been a Full Professor at the Department of

Mathematics, University of North Carolina at Charlotte. His research interest includes computational electromagnetics for parameter extraction for computer packaging and very large scale integrated (VLSI) designs and photonic waveguides.



Pingwen Zhang received the Ph.D. degree in computational mathematics from Peking University, Beijing, China, in 1992.

From 1992 to 1994, he was an Assistant Professor in the School of Mathematical Science, Peking University. In 1994, he became an Associate Professor. Since 1996, he has been a Professor. He is the Director of the School of Mathematical Science and the Executive Deputy Director of Center for Computational Science and Engineering, Peking University.

He is also the Vice Chairman of the China Society for Computational Mathematics. His research interests include multiscale modeling, analysis and computational method, and computational mathematics and its application.

Dr. Zhang received the Medallist of Wu'si Youth Award, the National Science Fund for Distinguished Young Scholars, and Changjiang Professor in 2002. He is an Executive Editor of the *Journal of Computational Mathematics* (in Chinese) and the *Journal of Computational Physics* (in Chinese). He is also an Associate Editor of the *Communications in Mathematical Sciences*.